Elucidating the Mechanism of Fatigue Crack Acceleration Following the Occurrence of an Underload

Article *in* Advanced Engineering Materials · July 2016

DOI: 10.1002/adem.201600069

7 authors, including:

Enrico Salvati
University of Oxford
47 PUBLICATIONS **186** CITATIONS

SEE PROFILE

Tan Sui
University of Surrey
85 PUBLICATIONS **402** CITATIONS

SEE PROFILE

Alexander Lunt
University of Bath
43 PUBLICATIONS **257** CITATIONS

SEE PROFILE

ADVANCED ENGINEERING MATERIALS

DOI: 10.1002/adem.201600069

Elucidating the Mechanism of Fatigue Crack Acceleration Following the Occurrence of an Underload**

By *Enrico Salvati,* Tan Sui, Hongjia Zhang, Alexander J. G. Lunt, Kai Soon Fong, Xu Song* and *Alexander M. Korsunsky*

Fatigue Crack Growth Rate (FCGR) is altered by a single anomalous load exceeding cyclic maximum (Overload) or compressive load below cyclic minimum (Underload). The authors study fatigue crack acceleration due to a single compressive Underload using residual stress mapping (by synchrotron XRD) and crack closure analysis (by DIC). The relative influence and duration of these two principal causes of FCGR alteration are revealed. Validated FEA model is used for parametric analysis of the effect of baseline cyclic loading ratio and magnitude of Underload on the cyclic J-integral.

1. Introduction

In recent decades, great effort has been devoted by the research community to understanding fatigue crack growth behavior in mechanical components subjected to variable amplitude loading.[1–3] No agreement has emerged so far regarding the best approach to crack growth prediction under this loading mode,[4] due to the difficulties in understanding the exact role of plasticity-induced crack closure,[5] residual stress generated ahead the crack tip,[6] and other mechanisms[7–9] that control crack propagation.

A single anomalous load encountered during constant amplitude fatigue test can be thought of as the simplest case of variable amplitude loading. Material response under variable amplitude fatigue can, therefore, be initially explored through the analysis of a single Overload (OL), single Underload (UL), or their combination (e.g., OL–UL).

In recent years, publications devoted to this topic largely concerned cases of OL.[10–13] It is well known that the application of an anomalous OL during constant amplitude fatigue test induces crack growth retardation during the propagation through the affected region. Even though some disputes persist regarding the contribution made by different mechanisms, this retardation is thought to be associated mainly with the effect of plasticity-induced crack closure, and the amplification of the compressive residual stress ahead of the crack tip.

When an UL is applied, observations show either crack growth acceleration, or no detectable disturbance in the FCGR.[14–16] This crack acceleration effect was noted in pipelines subjected to varying internal pressure.[17] It has been noted[15] that crack acceleration is likely to be manifested in cases where the baseline fatigue loading is positive, i.e., positive loading ratio R. Furthermore, higher crack acceleration occurs at higher baseline loading ratio.[18] In addition, the extent of such acceleration, if present, is dependent on the material cyclic hardening behavior and the magnitude of UL with respect to the steady-state cyclic load.

Using reasoning similar to that used for the analysis of OL, it is possible to anticipate that the main causes of the UL effect may be two contributions: the plasticity-induced crack closure effect and the change in the sign of residual stress acting ahead of the crack tip due to the UL application. While the OL magnifies the compressive residual stress acting ahead of the crack tip, the application of UL is likely to create a region of tensile residual stress or at least modifies the positive stress intensity factor toward greater magnitudes. It follows an increasing of the mean stress acting at the crack tip leading to the consequent reduction of fatigue life.

The crack closure effect[5] is caused by the contact between crack faces that occurs at loads exceeding the cyclic minimum, leading to the reduction of the stress intensity factor range. This effect is known to increase monotonically during crack propagation under constant amplitude fatigue; leading to rise of the minimum load required in order to separate the crack flanks as the crack advances.[19] The consideration of crack closure leads to the widely accepted method for calculating

[*] *E. Salvati, Dr. T. Sui, H. Zhang, Dr. A. J. G. Lunt, K. S. Fong, Dr. X. Song, Dr. A. M. Korsunsky*
Department of Engineering Science, University of Oxford, Parks Road, Oxford OX1 3PJ, United Kingdom
E-mail: enrico.salvati@eng.ox.ac.uk

[**] *AMK acknowledges funding received for the MBLEM laboratory at Oxford through EU FP7 project iSTRESS (604646), and access to the facilities at the Research Complex at Harwell (RCaH), under the Centre for In situ Processing Studies (CIPS). The authors have declared no conflict of interest.*

the effective Stress Intensity Factor (SIF) range. An important exception is the case of high values of the loading ratio R at which closure may not occur.[20] The crack closure level can be altered by the application of a single anomalous load. In the specific case of UL, this is likely to reduce the crack closure level[16,21] leading to the increase in the effective SIF and causing crack acceleration. Closure is also known to depend on the crack surface roughness and the nature of the asperities present (hard vs. soft), thus related to the mechanical behavior of the material volumes residing at crack surfaces, such as the presence of different phases and the extent of strain hardening.

Since OL is known to lead to crack tip blunting, one may surmise that UL may have the opposite effect, i.e., induce crack sharpening. However, experimental consideration appears to show the opposite effect, i.e., that crack tip tends to blunt, although by an amount that is more limited than due to OL.[22]

In order to obtain a better understanding of the causes of crack acceleration due to UL and to assess their contribution, in this study we use the combination of modern mechanical microscopy techniques, namely, Synchrotron X-ray Powder Diffraction (SXRPD) for residual and "live" strain mapping, Digital Image Correlation (DIC) for "live" deformation monitoring and three-dimensional Finite Element Method (FEM) for numerical modeling strain evolution during relevant instants of the crack propagation.

Our proposed strategy consists of the analysis of the strain field evolution in the course of an UL application. We also wish to address and resolve the disagreement that exists between published reports regarding the dependence of the FCGR acceleration as a function of the amplitude of the baseline fatigue load. To this end, we analyze the strain field variation following the application of UL using non-linear FEM analysis. Furthermore, the crack closure effect was visualized directly by means of DIC analysis of the relative displacement of crack faces, allowing explicit evidence to be extracted and presented.[23–24] DIC was used to record the crack flanks relative displacement using a sequence of images of the crack tip and its near wake acquired during fatigue test. The correlation between these images and the instantaneous applied load provides a means of direct evaluation of the crack opening load, and the calculation of the reduction in the effective Stress Intensity Factor.

Fatigue tests were carried out using mini-Compact Tension (CT) samples extracted from a rolled plate of Mg alloy AZ31b A samples was first subjected to cyclic constant amplitude loading at the load ratio $R = 0.1$. After crack was nucleated and propagated, a single UL was applied to the sample. Two additional samples were tested at constant amplitude until failure occurred in order to provide a baseline for comparing the behavior of the UL sample behavior. In the case of strain field assessment around the crack tip, a sample was firstly fatigued at constant load amplitude and before the UL application, a single OL was applied to the sample. The strain mappings were performed using synchrotron diffraction (SXRPD) prior, during and after the UL application. SXRPD has been used in previous studies for the characterization of the stress field,[25–28] in particular around the crack tip during crack propagation and at the occurrence of an overload.[29–33] This method allows high spatial resolution observation of the elastic strain state surrounding the crack tip, the identification of the plastic zone, and monitoring its evolution during subsequent crack propagation. The high energy and flux provided by synchrotron X-ray beam ensure that the experimental data collection was carried out in transmission mode. Therefore, the subsequent strain analysis is performed on the bulk of the sample, allowing fast data collection and the construction of two-dimensional strain maps of the area of interest at the crack tip. We focus our attention particularly on the visualization of the strain component parallel to the loading direction.

The purpose of carrying out FEM analysis in the first instance was to comparing numerical predictions with experimental observation and then validate the simulation approach. The validated model was firstly used to perform parametric analysis varying the baseline fatigue load in terms of loading ratio keeping constant the loading range. Secondly, the effect of the underload magnitude was also explored through an additional parametrical analysis. As output of these simulations, the computed J-integral was considered to be representative of the material propensity to crack propagation. Therefore, in the loading cycle following the underload, the J-integral range and its mean value were computed; these values formed the basis for discussion and observation of the results.

2. Fatigue Test and Material Description

2.1. Material Description and Crack Propagation Test

The material of choice for the experiment outlined in the previous section must fulfil a number of requirements in order for meaningful results to be obtained. Firstly, sufficient amount of ductility is required, since it enhances the effect of retardation/acceleration due to OL/UL through the creation of large plastic zone. This must be balanced against stiffness to ensure sufficiently high magnitude of yield strain, which in turn produces high values of elastic strain at the crack tip that are more easily measurable keeping errors low. Secondly, high-resolution SXRPD requires the material to be suitably fine-grained to ensure good polycrystal averaging over multiple grains of many possible orientations within the gauge volume to give rise to smooth powder diffraction patterns that lend themselves naturally to interpretation. Magnesium alloy AZ31b subjected to severe plastic deformation by Constrained Groove Pressing (CGP), under controlled temperature conditions in order to promote re-crystallization, possesses a refined grain size in the micron range, and displays an increase in tensile strength with respect to the base heat treatment, without compromising toughness.[34–35] The resulting favorable combination of properties is characterized by the yield stress is of $\sigma_y \approx 260$ MPa, 10% of total elongation

ADVANCED ENGINEERING MATERIALS 2016,
DOI: 10.1002/adem.201600069

and the grain size distributed in the range from <1 to 5 μm maximum. Previous work has been carried out and reported concerning fatigue crack growth behavior of this alloy under variable loading history, the overload (OL) effect in particular,[36] confirming the feasibility of the experiment proposed presently.

A 2 mm-thick miniature Compact Tension (CT) specimen (35 mm) was used for fatigue testing. The same sample geometry was successfully adopted in a previous publication.[10] Cyclic loading was applied using a servo-hydraulic fatigue rig capable of applying cyclic loading up to 20 kN. The baseline constant amplitude fatigue loading was performed at the frequency of 7 Hz. Simultaneously, the crack progression length was monitored and recorded using an optical microscope system providing images having pixel size of around 1 μm, allowing precise determination of the crack length and evaluation of fatigue crack growth rate (FCGR), and video recording of the crack opening and closure for subsequent DIC interpretation. The fatigue test setup is depicted in Figure 1a.

Four samples were employed in the experiment. Two samples denoted s.1 and s.2 were cyclically loaded at constant amplitude until complete sample fracture occurred. The cyclic loading ranged from the minimum load of $F_{min} = 80$ N to the maximum load $F_{max} = 800$ N, with the load ratio R equal to 0.1. The sample (s.3) was cyclically loaded until it had reached the crack length of 4.5 mm when an UL was applied having magnitude of $F_{UL,1} = -1\,200$ N. Further constant amplitude fatigue loading allowed the assessment of crack propagation rate as the crack advanced. During the whole fatigue test, images of the crack flanks were taken with the purpose of performing DIC analysis. The load history is summarized in Figure 1b. A fourth sample (s.4) was tested at the same fatigue baseline as the two baseline samples, but subjected to a single overload (OL) of $F_{OL} = 1\,200$ N followed by an Underload (UL) $F_{UL,2} = -960$ N when the crack length reached 4.5 mm, as illustrated in Figure 1c. Such particular loading history was chosen in order to validate the numerical model in an extreme situation where both anomalities (OL/UL) are present. The OL/UL application was in situ during the SXRPD experiment; a miniature tensile loading stage provided by Deben was used. The strain field around the crack tip was mapped at various loading levels. A single UL of magnitude was applied. The UL ratio defined as the FUL divided by the maximum value of the baseline cyclic loading F_{max} was equal to $R_{UL} = -1.2$.

2.2. Crack Propagation Results

The monitoring of the crack length as a function of the number of cycles during the fatigue test allowed the evaluation of crack growth rate variation with the applied stress intensity factor range. As seen in Figure 2a, in the case of the sample subjected to UL, a brief acceleration of the crack propagation rate was observed. The UL induced an instantaneous increase in the propagation rate. Using the SIF formulation found in Murakami et al.,[37] the fatigue crack growth rate (FCGR) and related Paris' curve were constructed (Figure 2b). The plots in Figure 2 incorporate the data from the totality of the tested samples. Fatigue crack growth rate (FCGR) acceleration is apparent. The FCGR plot in Figure 2b provides the basis for quantitative evaluation of the duration of acceleration effect, as it becomes apparent when the effect of UL vanishes and the steady-state condition is re-established. Quantitative analysis reveals that the FCGR alteration persists over 0.57 mm crack advance following the UL application. A close-up plot of the FCGR is shown in

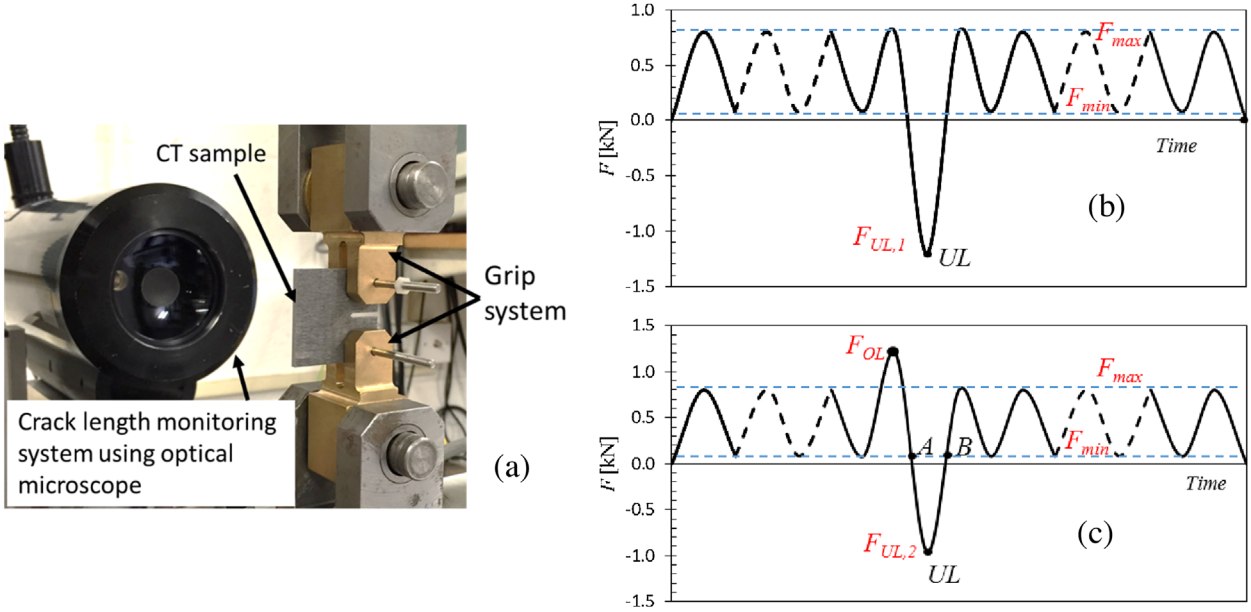

Fig. 1. (a) Test setup arrangement, (c) fatigue loading history sample s.3 (c) and fatigue loading history sample s.4.

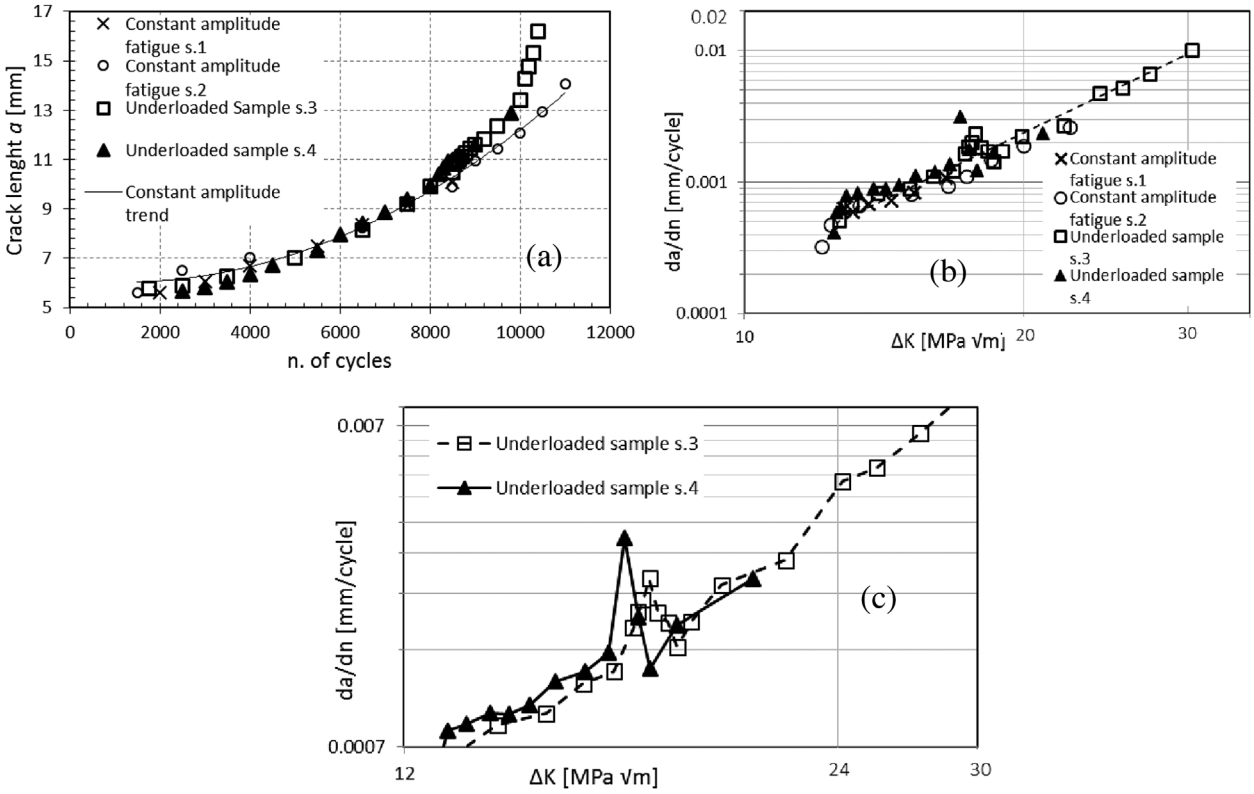

Fig. 2. Fatigue crack propagation results. (a) Crack length versus n of cycles (b) Fatigue Crack Growth Rate (FCGR) versus SIF range, and (c) enlargement of the FCGR versus SIF range at the occurrence of the underloads for samples s.3 and s.4.

Figure 2c where the sample subjected to UL and OL/UL were plot exclusively; this helps visualizing the difference between the two.

The two samples tested under steady-state constant cyclic amplitude conditions (s.1 and s.2) were used to extract the power law fit to the FCGR versus ΔK dependence, leading to the Paris' law expression (Eq. 1) for this material:

$$\frac{da}{dn} = C\,\Delta K^{m}, \tag{1}$$

in which the coefficients C and m were found to be equal to 2×10^{-7} [mm (cycle MPa $\sqrt{\text{m}})^{-1}$] and 3.21, respectively. The line corresponding to the above equation is shown dashed in Figure 2b.

3. Strain Field Evaluation

3.1. SXRPD Experimental Setup

In order to map the distribution of strain at the crack tip, three sets of measurements were performed at various loading conditions. Sample s.3 used in the SXRPD experiment was mounted upright in the Deben miniature tension-compression stage capable of applying load up to ±5 kN. A small segment of the loading history reported in Figure 1b around the UL application were reproduced in situ, with the three conditions of measurement identified as *A* (before underload), *UL* (during underload), and *B* (one cycle following the underload).

The strain maps at the crack tip were constructed using SXRPD strain analysis. The experiment was performed at Test Beamline B16 at the UK synchrotron facility, Diamond Light Source (DLS) located at Harwell Oxford (UK). Given the sample thickness of 2 mm, the high flux, high-energy beam provided by Synchrotron X-ray was used to perform the test in transmission mode. In this modality of mechanical microscopy, the diffraction patterns obtained provided averaged information about the lattice parameter variation through the entire sample thickness. The X-ray energy used was 20 keV and the beam size 45 μm × 45 μm.

The sample arrangement is shown in Figure 3. The sample was placed in the upright configuration with respect to the tensile stage, so that contemporaneous load application and beam mapping was possible. The tensile stage was placed on a beamline translation stage in order to allow the movement required for the scanning along the x and y laboratory coordinate axes defined according to Figure 3, (z-axis associated with the incident X-ray beam, x-axis horizontal and y-axis vertical in the plane perpendicular to the incident beam). 2D diffraction patterns consisting of sharp and smooth Debye–Scherrer rings were acquired by means of a Photonic Science X-ray Image Star 9000 detector.

DOI: 10.1002/adem.201600069

ADVANCED ENGINEERING MATERIALS

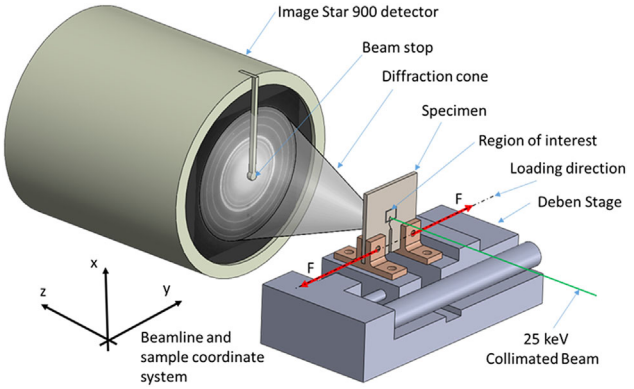

Fig. 3. Experimental setup indicating the coordinate system, principal experimental devices adopted and sample orientation.

3.2. SXRPD Strain Mapping

In order to determine the strain field map around the crack tip from the acquired diffraction patterns, azimuthal integration (binning) of Debye–Scherrer rings was performed for the grain family corresponding to the reflection with the Miller index (20.0) of the hcp structure of magnesium alloy AZ31b. The strain component aligned with the loading direction was sought by integrating the sector of the ring within the range ±30°. The adoption of such sector of integration leads to a maximum relative error of ≈8.5% in strain determination in terms of the maximum difference between principal strains. In the present case, the analyzed strain component is considered be one of the in-plane principal strains. Following binning to obtain the equivalent 1D X-ray diffraction profile as function of the diffraction angle 2Θ, the variation of lattice spacing Δd was evaluated throughout the scan, and used as input in the differential form of Bragg's law that allows the strain to be determined as follows:

$$\varepsilon_{yy} = \frac{\Delta d}{d_o} \tag{2}$$

As is well known, the determination of strain using the above formula requires the knowledge of the strain-free lattice parameter d_0 that denotes the distance between crystal planes in the unstrained condition. Such parameter is not always easy to be determined, since a priori knowledge of the location where the value of strain approaches zero or a known value is problematic, the use of powdered sample is fraught with difficulties of preserving identical scattering conditions and sample-to-detector distance, and solute chemistry variations due to heat treatment history may cause the variation of lattice parameter compared to the literature values for the material studied. The strategy adopted in order to overcome this issue was to rely on the use of FEM as a modeling in order to obtain most reliable matching of simulation to observation, while considering d_0 as a fitting parameter to minimize the disagreement. More specifically, the predicted strain field was considered in a region lying sufficiently far away from the crack tip not to be affected by local plasticity, yet sustaining measurable elastic strain. Further matching with the numerical model allowed the refining of d_0 that turned to be 0.244 nm. Therefore, this value was used to determine the magnitude of experimentally measured strain field at any point on the maps.

A Matlab routine was used for the analysis of 1D diffraction patterns. For each experimental position the (20.0) reflection was fitted with a Gaussian peak curve, and the relative change in the lattice spacing corresponding to the peak center was calculated. Strain maps were constructed in Matlab. The d_0 was then varied seeking the best match of these results with the numerical prediction along the crack bisector.

3.3. FEM Analysis

Since the experimental strain field mapping is the average value along the sample thickness, the modeling of crack growth cannot be performed under the simplification of plane-stress or plane-strain. To better reproduce the real case, a three-dimensional FEM analysis was performed with the purpose of capturing the strain field variation through the thickness of the sample. Given the importance of accurately represent the material hardening behavior within the FEM software, a combined hardening rule was implemented. Such rule provides the description of the kinematic hardening rule by means of the Chaboche model[38] and the cyclic softening/hardening behavior by superposition of an isotropic hardening rule as described in Chaboche and Leimatre.[39] This model required an accurate calibration that was accomplished using a supplementary model where cyclic behavior was simulated and, by matching the result with the experiment, the model's coefficients were found. The kinematic part was calibrated using two backstresses. Values of the combined kinematic/isotropic model found are summarized in Table 1

Regarding the kinematic part, the coefficients C indicate the slope of the hardening rule and γ is the rate at which the kinematic component approaches its asymptote. As far as the isotropic rule is concerned, the parameter Q_∞ is the asymptotic value of strain hardeinig/softening and b is the rate at which the isotropic component approaches its asymptote.

A quarter of the CT sample was modeled taking advantage of the symmetries in order to minimize the computational effort. The 8-node linear brick elements were used for the discretization of the model. The mesh convergence allowed the finding of a good compromise between the computational speed and result quality. The half thickness of the sample was subdivided in n.6 elements, the elements present at the vicinity of the crack wake were made 0.1 mm × 0.02 mm and,

Table 1. Combined hardening rule coefficients.

C_1[MPa]	γ_1	C_2[MPa]	γ_2	Q_∞[MPa]	b
90 000	9 000	600	3	50	2

FULL PAPER

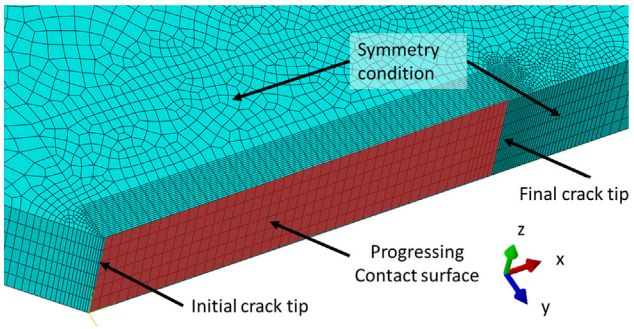

Fig. 4. Model discretization. Detail of the mesh refinement along the crack propagation path.

at the OL/UL application site, the mesh elements were 0.02 mm × 0.02 mm as depicted in Figure 4. In total, the model was constituted of 27 000 elements.

The strain evolution, as the crack propagated through the sample, was simulated by considering several propagation steps from the nucleation until the final stage. The crack propagation was subdivided in n.12 steps. The first 10 steps after crack nucleation were equispaced of 0.4 mm and the last two steps were 0.3 and 0.2 mm, respectively. At each propagation step, the cyclic load was applied to simulate the material cyclic response. In order to capture the crack flanks contact and, thus, the induced plasticity crack closure, an hard contact was modeled at the surface where the contact could happen as shown in Figure 4. The modeled contact was of the type "Hard" with the method "Augmented Lagrange."

3.4. SXRPD Results and FEM Model Validation

After matching the numerical outcomes with the experimental ones by refining of the material d_0, the obtained maps can be plotted. Figure 5 shows contour plots for the three instants of loading (*A*, *UL*, *B*) considered. Note that the crack tip is not always located at the center of the figure as a consequence of the choice of experimental setup. The crack tip location is indicated by the wedge-shaped black lines on the left of each map and, after rough estimation, it was precisely localized by matching with numerical model.

In the first map shown in Figure 5a, the region of interest in the strain field surrounding the crack tip has been captured. The strain field at the application of the UL is revealed in fine detail in Figure 5b.

Compressive strain ahead the tip was detected in all the loading steps. As expected, at the occurrence of the UL, high magnitude of compressive strain was generated, and a steep gradient of strain ahead of the crack tip was observed.

It is worth noting that ahead of the crack tip in the cases before and after the UL in Figure 5a and c, a small jump can be observed along the crack bisector, producing a sort of banding effect in the maps (circled by dashed line in Figure 4c). This suggests that a pre-existent background residual strain may persist in the material arising from the previous severe plastic deformation during material forming.

The comparison of the strain fields obtained is reported in Figure 6 as line plots along the crack bisector. The experimental results are shown along with the error bands at 95% of confidence arising from the error of peak position obtained from the Gaussian fitting of the diffraction peaks, propagated to calculate the strain uncertainty.

The comparison between the experimental and numerical results shows satisfactory overall match in terms of the trend in strain variation. Even in terms of strain magnitudes, the numerical predictions appear to match the experimental profiles. Unfortunately, the strain field ahead the crack tip for the loading condition A (Figure 1b) shown in Figure 6a, cannot be verified due to lack of experimental points.

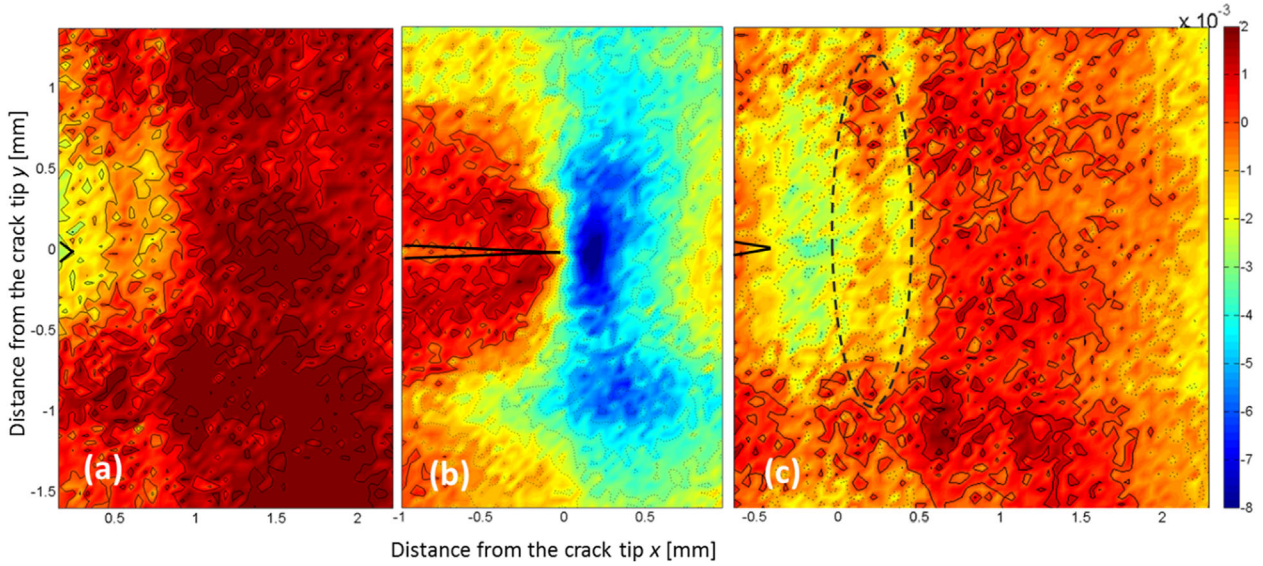

Fig. 5. Strain contour map ε_{yy} obtained by SXRD. (a) Before (instant A) (b) during (instant UL), and (c) after (instant B) UL application.

DOI: 10.1002/adem.201600069

ADVANCED ENGINEERING MATERIALS

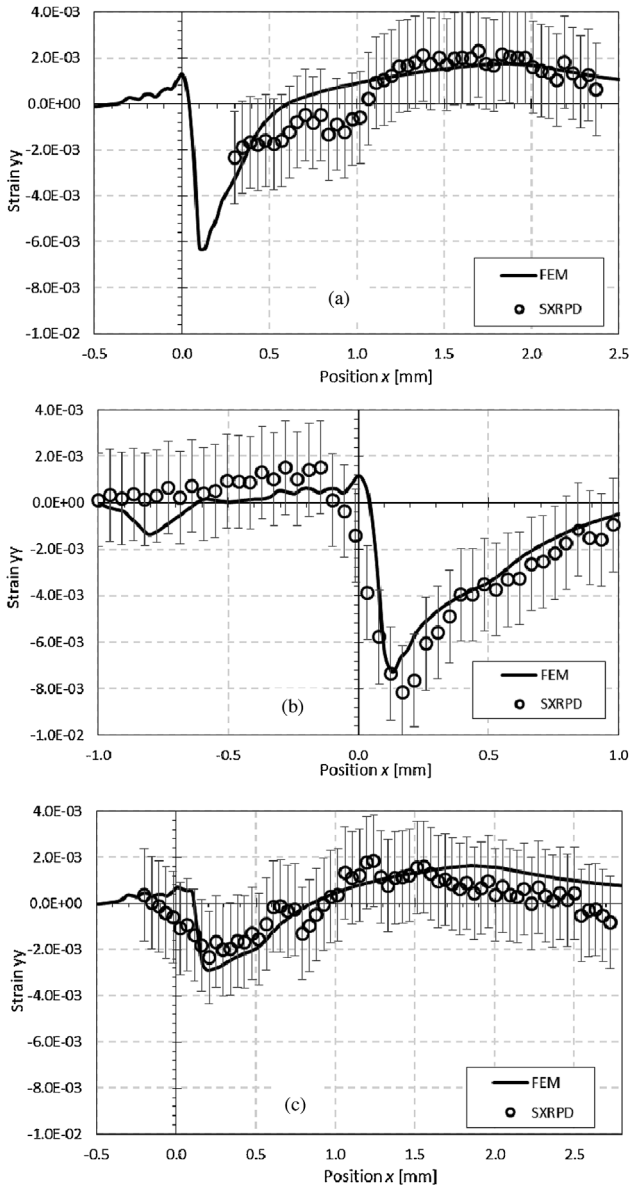

Fig. 6. Experimental versus FEM results of the elastic strain in the direction of the external load ε_{yy}. The origin of the x-axis indicates the crack tip position. Comparison along the crack bisector (a) before UL (instant A) (b) during UL (instant UL), and (c) after UL (instant B).

On the basis of the results presented in this section, we draw the conclusion that satisfactory validation has been obtained of the numerical approach selected, and that it can be adopted for further analysis of UL effects on FCGR.

3.5. FEM Parametric Analysis

To advance the understanding of how the crack growth is affected by the cyclic loading and the magnitude of the UL, several parametric analyses were performed. In the elastoplastic regime, one of the effective parameter that can be used as representative of the crack driving force is the J-integral.[40–42] This parameter is known to be efficient in accounting also the effect of crack closure,[43] therefore we used such J-integral, in particular its range within each cycle, for the assessment of the crack driving force change as the UL magnitude and baseline loading vary. The cyclic J-integral was then evaluated at the cycle that follows the UL application in each simulation. The computation of the J-integral value was performed at the distance of 0.5 mm from the free surface of the sample in order to obtain a good compromise between the plane-stress condition (free surface) and the quasi-plane-strain condition (mid-thickness). The path of integration was chosen wide enough with the purpose of avoiding artifacts that may arise from the crack tip plastic zone. The Modified Monotonic Loading (MML) method was used for the cyclic J-integral calculation. This method provides a reasonable approximation of the crack driving force parameter.

The first parametric analysis was focused on the evaluation of the UL magnitude effect on the variation in J integral range ΔJ. The cyclic fatigue loading was kept constant and it was the same as shown in Figure 1b. Along with the range, the mean value was also monitored, since it may play an important role on fatigue damage. Therefore, the mean value of J-integral in the cyclic loading and the ratio defined as the minimum value divided by the maximum value ($R_J = J_{min}/J_{max}$) were assessed. With this end, n.7 analysis was performed. The Figure 7 shows the variation of both the mean value J_{mean} and the range ΔJ.

Regarding the effect of the baseline fatigue loading, we studied several cases where the loading range applied to the sample was kept constant equal to the above shown analysis $\Delta F = 720$ N and the variable was set to be the external loading ratio R. The results are shown below in Figure 8.

4. Crack Closure Analysis

As previously discussed in reference to previous publications, crack acceleration may occur mainly due to the combination of tensile residual stress with the change in the crack closure level. Here, we analyze how the crack closure mechanism deviates from the steady-state trend after an UL occurs.

The fatigue test setup used in the present study allowed capturing a sequence of detailed images of the crack tip and wake during cyclic test at low frequency (0.1 Hz). As successfully previously conducted by other researcher,[44–48] a DIC analysis is able to capture the crack flanks relative displacements. Using a Matlab-based DIC software,[49] this relative crack flank displacement, also known as the Crack Opening Displacement (COD), was monitored at the distance of 0.25 mm behind the crack tip toward its wake. Such analysis was performed once the crack had reached different lengths: 7.73, 8.18, 8.56, 9.09, 9.65, 10.35 mm (before UL); 10.35 mm (at UL); and 10.52, 10.84, 11.01 mm (after UL).

An example the COD behavior in the presence of crack closure is reported in Figure 9a, where the COD is plotted together with the applied load, so that the direct comparison is possible. The COD follows the sinusoidal profile of the applied load very well while the magnitude of applied load

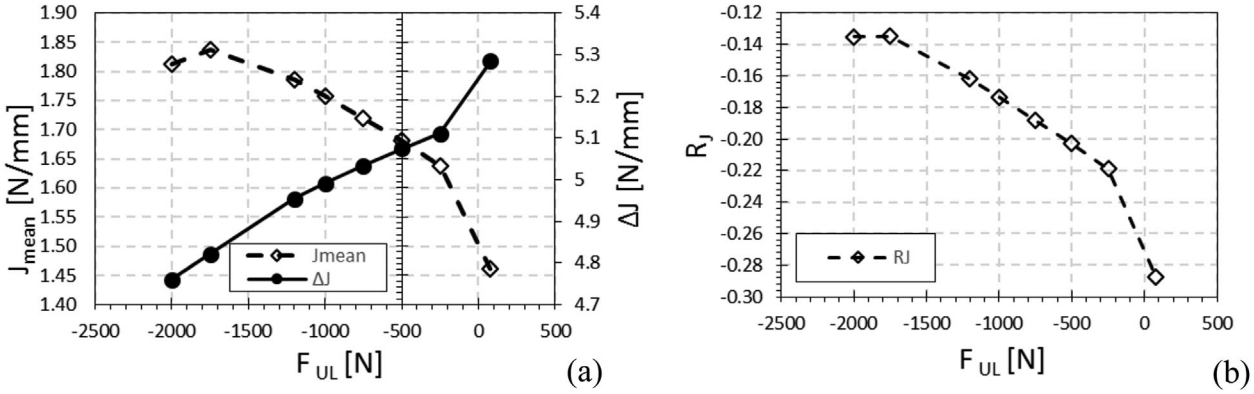

Fig. 7. Parametric analysis results for the variation of the magnitude of UL. Plots show the variation of (a) the mean value J_{mean} and the range ΔJ of the J-integral, and (b) of the J-integral ratio R_J.

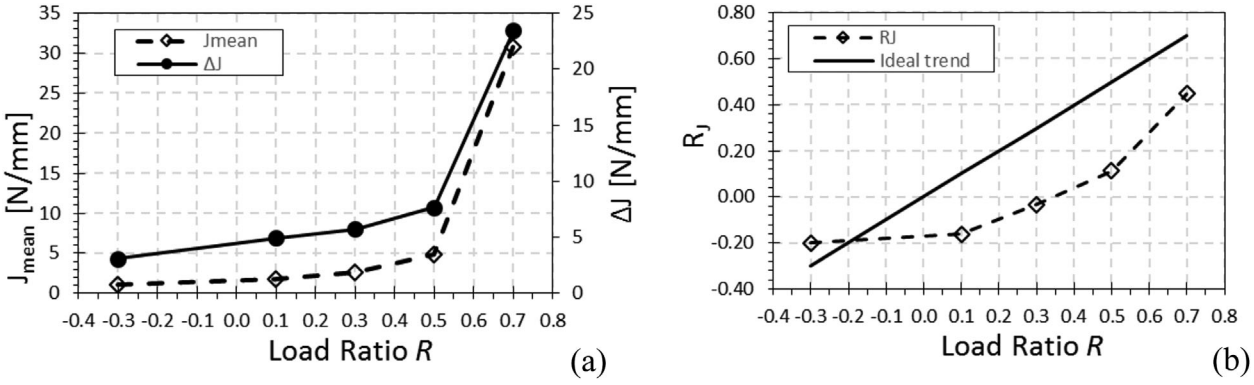

Fig. 8. Parametric analysis results varying the baseline loading ratio. (a) Mean value J_{mean} and range ΔJ of the J-integral plot and (b) J-integral ratio R_J plot.

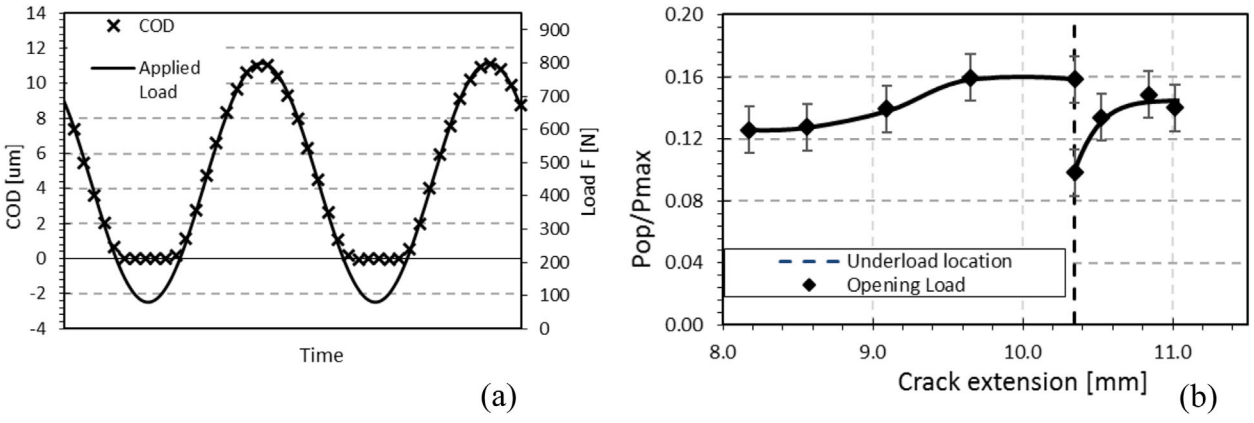

Fig. 9. Crack closure analysis. (a) Example of simultaneous crack opening displacement and applied load plots example at crack length a = 2.577 mm. (b) and normalized opening load plot during crack propagation.

remains high. However, in the course of unloading, the COD reduces to its minimum value of zero *before* the load reaches the cyclic minimum, as the flanks come into contact that does not allow any further relative movement. The most important bit of information that can be extracted from this type of graph is the crack opening load denoted F_{op} below, i.e., the value of load at which the crack flanks first come into contact during unloading part of the cycle, or separate under increasing load. For example, for the case shown in Figure 9a crack closure occurs at around 200 N of applied external force. In the majority of the cases, the opening load is correspondent to the closure load (an example is given in Figure 9a).

The opening load can be used for the calculation of the opening stress intensity factor, and hence the effective stress

DOI: 10.1002/adem.201600069

ADVANCED ENGINEERING MATERIALS

intensity factor. For the purpose of exploring the variation in crack closure level as the crack moves past the UL region, we report the normalized opening load as a function of the crack length in Figure 9b.

The opening load was normalized with respect to the maximum load (800 N). The error arising from the calculation of the opening load was estimated, and is reported using error bands at 95% confidence. As Figure 9b shows, at small crack lengths the crack closure ratio was around 0.13. As the crack propagates this value increases gradually until it reaches the value of 0.16 immediately prior to the UL application. After UL occurs, a clear drop in the crack closure ratio is observed, down to the value of 0.10, or 37.5% lower. The prompt return of the FCGR to the steady-state condition is here confirmed by the fact that after ≈0.5 mm of further crack propagation the crack closure ratio returns to the value ≈0.15.

The opening load could be used directly for the calculation of the actual FCGR, by computing the effective SIF at the crack tip as

$$\Delta K_{\text{eff}} = K_{\max} - K_{\text{op}} \tag{3}$$

Here K_{op} is the SIF at the opening load F_{op}, and $K_{\max}$ is the SIF when the load reaches its maximum value during cycling. The effective SIF ΔK_{eff}, according to the DIC closure analysis, was reconstructed and plotted against the FCGR (Figure 10).

The reduction of K_{op} leads to an enhancement of the effective SIF and subsequent crack acceleration. In fact, in Figure 10 it is possible to note that the alteration given by the UL (acceleration) that was clearly visible in the plot in Figure 2c it is now attenuated by correcting the closure effect. Further implications of these findings are discussed in the following section.

5. Discussion

Fatigue test involving the application of a single peak compressive underload (UL) were used to explore the crack acceleration effect that persists over a certain range of subsequent crack extension (sample s.3). Alongside this test, a more complex loading history was applied to an additional CT sample for the in-situ measurement of the strain evolution (sample s.4).

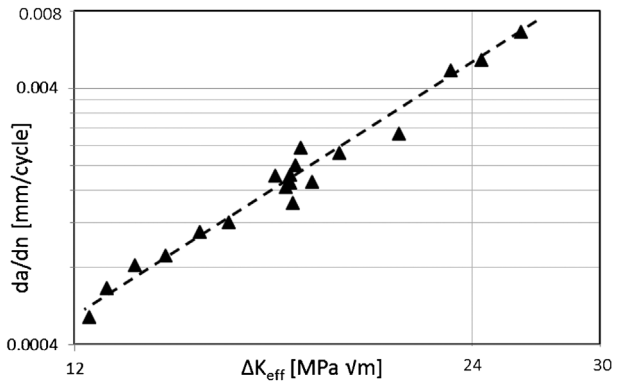

Fig. 10. Effective Stress Intensity factor plot relative to the analyzed sample s.3.

In both the experimental tests, where OL and/or UL were involved, crack acceleration was experienced. The results summarized in Figure 2, specifically in the close-up in Figure 2c, have highlighted two slightly type of accelerations. In the case of sample s.3 (no OL), even though the UL magnitude was greater that the case of sample s.4, the effect of retardation in terms of FCGR was of smaller magnitude. On the other hand, if we consider the extension of such retardation, then we can certainly say that for the sample s.3 it persist for longer crack propagation length. This effect may be due to the interaction of OL/UL that produced a great acceleration at the first stages of propagation and a quick restoration to the steady-state regime. In fact, in some cases the sole occurrence of an OL may create a short acceleration preceding a more persisting retardation region.

Supporting experimental measurements of the strain fields were mainly aimed at the validation of a three-dimensional FE model. Such FE model allowed the identification of the role of strain field change ahead of the crack tip and the modification of the crack closure effect that were identified as the crucial determining mechanisms that caused the observed phenomena.

Crack acceleration is believed to be associated with the tensile residual elastic strain (and stress) present immediately ahead of the crack tip, or with the reduction in the level of residual compression induced by the prior steady-state crack propagation stage. We attempted to capture this tensile strain region experimentally using SXRPD. No direct evidence of local tensile strain could be detected ahead the crack tip after the occurrence of UL but, a prominent change in the strain level was observed. Indeed, by comparing the Figure 6a and c, it is evident that the compressive strain peak ahead the crack tip was attenuated with the introduction of the UL.

However, the experimental result obtained was also used as the basis for developing and validating a numerical simulation based on FEM calculation that allowed parametric analysis to be conducted.

Two different parametric FE analyses were performed with the goal of evaluate the effect of the baseline cyclic loading, in terms of loading ratio R, and the magnitude of UL applied.

The analysis at constant baseline fatigue loading was performed at $R = 0.1$ at the same amplitude as shown in Figure 1b. As it is possible to see in Figure 7a, as the absolute magnitude of the UL increases, the range of J integral ΔJ decreases. For an UL, that varies from 80 to −2 500 N, the ΔJ varies of around 10%. Exactly the opposite trend can be observed for the mean value of J integral J_{mean}; in fact, as the UL absolute magnitude increase, the J_{mean} increases too. In the case of J_{mean}, the variation in the same range of UL change is of 24%. Another way of visualizing this is by plotting the local J integral ratio defined as $R_J = \frac{J_{\min}}{J_{\max}}$ as shown in Figure 7b. This led us to believe that in the case of $R = 0.1$, the crack acceleration is due to the drop of the mean value of J integral which is predominant to the increase of ΔJ.

DOI: 10.1002/adem.201600069

The second parametric analysis was conducted keeping constant both the magnitude of the UL ($F_{UL} = -1\,200$ N) and the load range $\Delta F = 720$ N, varying the load ratio R. In this instance both the J_{mean} and the ΔJ increase monotonically as the load ratio R grows, as shown in Figure 8a. Particularly, at high loading ratios (e.g., >0.5) the ΔJ is amplified of around one order of magnitude. Of course, this analysis does not attempt to capture how the ΔJ evolves during the further propagation, but surely right after the UL application for the first cycles the material is stressed more than the unaltered condition and thus more prone to promote crack propagation. The plot of the R_J against the external loading ratio for this analysis, shown in Figure 8b reveals also another important aspect. As we can see, the local R_J is reduced with respect of R when this last one is positive. This would let us to think that at $R>0$ the crack should be less prone to propagate when the UL is involved, but it is important to bear in mind that at the same time the range of J integral grows much faster as the R increases. Therefore, the conclusion is that the chance in loading ratio is reflected in greater part in the change of J integral range. Furthermore, high load ratios of the fatigue baseline enhance the effect of UL.

A graphical representation of the effect of the loading ratio R is shown in the Figure 11. These FEM contour images superimposed to the 6 × deformation amplification, provide some insights about the causes of such magnification of the ΔJ when high loading ratio of the baseline is involved. In the Figure 11a and b, we can see the crack status at the minimum load applied, before the UL, for two loading radio cases (i.e., $R = 0.7$ and $R = 0.1$). The following two Figure 11c and d show the strain and deformation status during the application of the UL (same magnitude), respectively, for $R = 0.7$ and $R = 0$. It is clear that, whereas the loading ratio is high, the UL produces much larger deformation at the crack tip compared with the one at $R = 0.1$. In fact, for $R = 0.1$ the majority of the deformation occurs at the notch root. This effect is due to the level of crack closure and blunting induced by the baseline. Indeed, the high F_{max} during cycling produced great level of blunting and closure that then allows this "pincer" effect at the crack tip when UL occurs. For low loading ratios, when the crack closes under the effect of the UL, the stresses are distributed along the crack flanks and not concentrated at the tip.

In is worth mentioning that, if the crack faces go in contact, the compressive forces that arise may flatten the asperities present and, as a consequence, the magnitude of the roughness-induced crack closure is reduced.

In summary, we observe the enhancement of tensile strain with increasing baseline load, and conclude that crack acceleration after UL is crucially dependent not on the UL magnitude, as might be surmised, but rather on the magnitude of the cyclic maximum load prior to the UL application. Our conclusion is in agreement with,[50] and is based on the advanced and detailed insight into the micro-mechanical processes at the tip of a growing fatigue crack.

Along side the residual stress at the crack tip, the plasticity induced crack closure is another mechanism that affects crack acceleration. To examine this hypothesis, the investigation of crack closure was conducted by means of DIC analysis. The crack closure/opening load ratio was evaluated at several crack propagation stages before and after the UL. Right after the UL the crack closure/opening load was reduced, as seen in Figure 9b. The effective SIF range ΔK_{eff} demonstrates that crack closure plays a crucial role in crack acceleration following UL. Also, the extent of the deviation in crack closure/opening load corresponds correctly to the length of crack propagation over which the acceleration is observed.

6. Conclusions

The work presented in this paper provides experimental and numerical evidence of the mechanisms that affect fatigue crack propagation past a compressive underload (UL). The strain field at the crack tip mapped by synchrotron X-ray diffraction was used for validating a numerical model of deformation. Experimental measurement revealed a limited reduction of the compressive strain experienced in the plastic region ahead of the crack tip. FEM parametric analysis showed that lower values of the baseline fatigue-loading ratio reduced the strain field alteration after UL and, if they were low enough, made the effect of UL negligible. The underlying mechanism behind this effect was explained considering the crack tip blunting and crack closure induced by the fatigue baseline load. Keeping the load range constant, it is possible to observe and enhancement of the crack closure and blunting effects when the loading ratio increases, which in turn has very significant impact on the effectiveness of the UL. It is worth highlighting that at low loading ratio the UL produces a great deal of

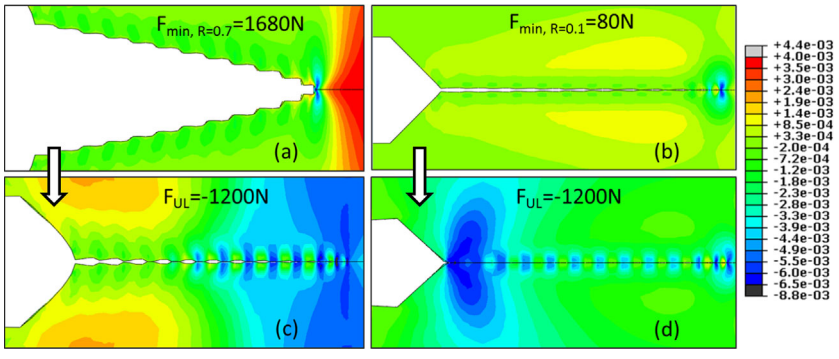

Fig. 11. Contour plots of the elastic strain component parallel to the load applied ε_{yy} at the relevant load conditions, plotted over the deformed geometry after the application of magnification factor (6×). (a) Before the application of the UL at the minimum load F_{min} in the case of load ratio $R = 0.7$. (b) Before the application of the UL at the minimum load F_{min} in the case of load ratio $R = 0.1$. (c) During the application of the UL right after the cyclic loading at $R = 0.7$. (d) During the application of the UL right after the cyclic loading at $R = 0.7$

ADVANCED ENGINEERING MATERIALS 2016,
DOI: 10.1002/adem.201600069

deformation along the crack faces and therefore the asperities are smoothed with a consequent reduction of the roughness induced crack closure effect. Regarding the influence of the UL magnitude on the crack driving force, it turns out to be less prominent that the baseline loading ratio. In fact, great variation in UL magnitude produces small change in the mean value of the cyclic J-integral.

Crack closure was monitored throughout crack propagation. The opening load displayed a sudden drop of 37.5% after UL application, and gradually returned to the steady-state value. The restoration of the unaltered crack closure state occurs at around 0.5 mm from the UL position, which is in agreement with the crack propagation length over which acceleration is observed. The drop in the opening load can be seen as an enhancement of the effective SIF range, and therefore provides a clear explanation for the acceleration effect observed.

In conclusion, the mechanisms that contribute to crack acceleration are mainly the crack tip blunting, crack closure, and the change in the residual stress state at the crack tip. The effect of the increase in the strain magnitude was not as obvious as that of the reduction in the opening load due to crack closure. This leads us to believe that the contribution given by crack closure is more significant and longer lasting than that of the near-crack tip plastic strain effect.

Article first published online: xxxx
Manuscript Revised: June 1, 2016
Manuscript Received: February 2, 2016

[1] A. Ray, R. Patankar, *Appl. Math. Model*. **2001**, *25*, 979.
[2] J. Zhang, S. Yang, J. Lin, *Fatigue Fract of Eng. Mater. Struct*. **2016**, *39*, 79.
[3] H. Liu, D. G. Shang, J. Z. Liu, Z. K. Guo, *Int. J. Fatigue* **2015**, *72*, 11.
[4] L. C. H. Ricardo, C. A. J. Miranda, *Frattura ed Integrità Strutturale* **2016**, *35*, 456.
[5] W. Elber, *Damage Tolerance in Aircraft Structures*. ASTM STP 486, American Society for Testing & Materials, Philadelphia PA **1971**, p. 230.
[6] A. Kumara, A. R. Murthya, N. R. Iyera, *Procedia Eng*. **2014**, *86*, 645.
[7] M. A. Meggiolaro, A. C. O. Miranda, J. T. P. Castro, L. F. Martha, *J. Fatigue* **2005**, *27*, 1398.
[8] D. J. Nicholls, *Fatigue Fract. Eng. Mater. Struct*. **1994**, *17*, 459.
[9] S. U. Khan, R. C. Alderliesten, R. Benedictus, *Compos. Sci. Technol*. **2009**, *69*, 2604.
[10] E. Salvati, S. O'Connor, T. Sui, D. Nowell, A. M. Korsunsky, A study of overload effect on fatigue crack propagation using EBSD, FIB–DIC and FEM methods. Engineering Fracture Mechanics, In Press, Corrected Proof, Available online 26 April 2016. doi: 10.1016/j.engfracmech.2016.04.034.
[11] R. L. Carlson, G. A. Kardometeas, P. R. Bates, *Int. J. Fatigue* **1991**, *13*, 453.
[12] K. Sadananda, A. K. Vasudevan, R. L. Holtz, E. U. Lee, *Int. J. Fatigue* **1999**, *21*, S233.
[13] W. Ochensberger, O. Kolednik, *Int. J. Fatigue* **2016**, *83*, 161.
[14] M. T. Yu, T. H. Topper, P. Au, in *Second International Conference on Fatique and Fracture Thresholds*, Chameleon Press, Birmingham UK **1984**, p. 179.
[15] F. S. Silva, *Int. J. Fatigue* **2007**, *29*, 1757.
[16] R. L. Carlson, G. A. Kardomateas, *Int. J. of Fatigue* **1994**, *16*, 141.
[17] M. Yu, W. Chen, R. Kania, G. Van Boven, J. Been, *Fatigue Fract. Eng. Mater. Struct*. **2015**, *38*, 681.
[18] M. Hassanipour, Y. Verreman, J. Lanteigne, J. Q. Chen, *Int. J. Fatigue* **2016**, *85*, 40.
[19] Y. Jiang, M. Feng, F. Ding, *Int. J. Plast*. **2005**, *21*, 1720.
[20] H. Tsukuda, H. Ogiyama, T. Shirais, *Fatigue Fruct. Eng. Mater. Struct*. **1995**, *18*, 503.
[21] V. Zitounisa, P. E. Irving, *Int. J. Fatigue* **2007**, *29*, 108.
[22] N. A. Fleck, *Acta Metall*. **1985**, *33*, 13339.
[23] D. Nowell, M. E. Kartal, F. P. Dematos, *Fatigue Fract. Eng. Mater. Struct*. **2013**, *36*, 3.
[24] D. Nowell, R. J. H. Paynter, P. F. P De Matos, *Fatigue Fract. Eng. Mater. Struct*. **2010**, *33*, 778.
[25] X. Song, M. Xie, F. Hofmann, T. S. Jun, T. Connolley, C. Reinhard, R. C. Atwood, L. Connor, M. Drakopoulos, S. Harding, A. M. Korsunsky, *Mater. Des.*, **2013**, *50*, 360.
[26] A. J. G. Lunt, N. Baimpas, E. Salvati, I. P. Dolbnya, T. Sui, S. Ying, H. Zhang, A. K. Kleppe, J. Dluhos, A. M. Korsunsky, *J. Strain Anal*. **2015**, 1, DOI: 10.1177/0309324715596700.
[27] A. M. Korsunsky, X. Song, F. Hofmann, B. Abbey, M. Xie, T. Connolley, C. Reinhard, R. C. Atwood, L. Connor, M. Drakopoulos, *Mater. Lett*. **2010**, *64*, 1724.
[28] N. Schalk, J. Keckes, C. Czettl, M. Burghammer, M. Penoy, C. Michotte, C. Mitterer, *Surf. Coat. Technol*. **2014**, *258*, 121.
[29] A. M. Korsunsky, X. Song, J. Belnoue, T. Jun, F. Hofmann, P. F. P. De Matos, D. Nowell, D. Dini, O. Aparicio-Blanco, M. J. Walsh, *In. J. Fat*. **2009**, *31*, 1771.
[30] P. Lopez-Crespo, A. Steuwer, T. Buslaps, Y. H. Tai, A. Lopez-Moreno, J. R. Yates, P. J. Withers, *Int. J. Fatigue* **2015**, *71*, 11.
[31] M. C. Croft, N. M. Jisrawi, Z. Zhong, R. L. Holtz, K. Sadananda, J. R. Skaritka, T. Tsakalakos, *Int. J. Fatigue*, **2007**, *29*, 1726.
[32] A. M. Korsunsky, X. Song, F. Hofmann, B. Abbey, M. Xie, T. Connolley, C. Reinhard, R. Atwood, L. Connor, M. Drakopoulos, *Diamond Light Source Proceedings*, Volume 1, Supplement SRMS-7, April **2011**, e107.
[33] J. P. Belnoue, T.-S. Jun, F. Hofmann, B. Abbey, A. M. Korsunsky, *Eng. Fract. Mech*. **2010**, *77*, 3216.
[34] K. S. Fong, D. Atsushi, T. M. Jen, B. W. Chua, *J. Manuf. Sci. Eng*. **2015**, *137*, 151004.

[35] K. S. Fong, D. Atsushi, T. M. Jen, B. W. Chua, *Procedia CIRP* **2015**, *26*, 449.
[36] S. Zheng, Q. Yu, Z. Gao, Y. Jiang, *Eng. Fract. Mech.* **2013**, *114*, 42.
[37] Y. Murakami, *Stress Intensity Factors Handbook Volume 2*, Pergamon Press, Oxford **1987**.
[38] J. L. Chaboche, V. Dang, G. Cordier, in *5th International Conference on Structural Mechanics in Reactor Technology* (Eds: A. Jeager, B. A. Boly), Bundesanstalt fur Material prufung, Berlin **1979**, 1.
[39] J. L. Chaboche, J. Leimatre, *Mechanics of Solids Materials*, Cambridge University Press, Cambridge, **1990**, ISBN 0-521-47758-1.
[40] D. Carka, C. M. Landis, *J. Appl. Mech.* **2011**, *78*, 011006.
[41] A. Ktari, N. Haddar, F. Rezai-Aria, H. F. Ayedi, *Eng. Fail. Anal.* **2016**, *66*, 354.
[42] T. Vojteka, J. Pokludaa, J. Horníkováa, P. Šanderaa, K. Slámečka, *Procedia Mater. Sci.* **2014**, *3*, 835.
[43] M. Metzger, T. Seifert, C. Schweizer, *Eng. Fract. Mech.* **2015**, *134*, 459.
[44] M. A. Sutton, W. Zhao, S. R. McNeill, J. D. Helm, R. S., W. T. Riddell, *ASTM STP* **1999**, *1343*, 145.
[45] P. F. P. deMatos, D. Nowell, *Int. J. Fatigue* **2009**, *31*, 1795.
[46] D. Nowell, P. F. P deMatos, *Procedia Eng.* **2010**, *2*, 1035.
[47] F. Yusof, P. Lopez-Crespo, P. J. Withers, *Int. J. Fatigue* **2013**, *56*, 17.
[48] S. Beretta, S. Rabbolini, A. Di-Bello, *Frattura ed Integrità Strutturale* **2015**, *33*, 174.
[49] C. Eberl, Digital Image Correlation and Tracking (Software). Web site (Nov. **2015**): http://www.mathworks.com/matlabcentral/fileexchange/12413-digital-image-correlation-and-tracking
[50] S. Y. Lee, Effects of Overload and Underload on Internal Strains/Stresses and Crack Closure during Fatigue-Crack Propagation. PhD diss., University of Tennessee, **2009**. http://trace.tennessee.edu/utk_graddiss/614

DOI: 10.1002/adem.201600069